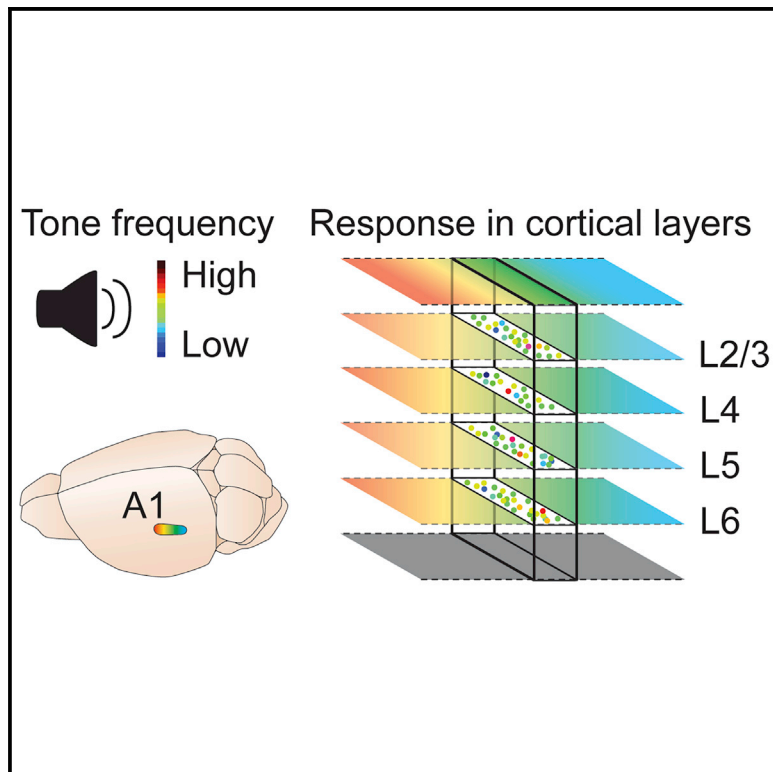


## In Vivo Functional Mapping of a Cortical Column at Single-Neuron Resolution

### Graphical Abstract



### Authors

Carsten H. Tischbirek, Takahiro Noda,  
Manabu Tohmi, Antje Birkner,  
Israel Nelken, Arthur Konnerth

### Correspondence

arthur.konnerth@tum.de

### In Brief

Tischbirek et al. report a two-photon  $\text{Ca}^{2+}$ -imaging-based approach to map sensory-evoked neuronal activity from L2/3 to L6 of mouse cortex. In the primary auditory cortex, the authors identify functional microcolumns at cellular resolution that bring together large-scale tonotopy and locally heterogeneous frequency responses throughout all cortical layers.

### Highlights

- Generation of a functional 3D map of a cortical column in mouse auditory cortex
- Local heterogeneity of best-frequency responses in all cortical layers
- Preserved tonotopy at cellular resolution in all cortical layers
- Similar micro-architecture for sound frequency representation in all cortical layers



# In Vivo Functional Mapping of a Cortical Column at Single-Neuron Resolution

Carsten H. Tischbirek,<sup>1,2,4</sup> Takahiro Noda,<sup>1,2,4</sup> Manabu Tohmi,<sup>1,2</sup> Antje Birkner,<sup>1,2</sup> Israel Nelken,<sup>3</sup> and Arthur Konnerth<sup>1,2,5,\*</sup>

<sup>1</sup>Institute for Neuroscience, Technical University of Munich, Munich, Germany

<sup>2</sup>Munich Cluster for Systems Neurology (SyNergy), Munich, Germany

<sup>3</sup>Department of Neurobiology, Silberman Institute of Life Sciences and Edmond and Lily Safra Center for Brain Sciences, Hebrew University of Jerusalem, Jerusalem, Israel

<sup>4</sup>These authors contributed equally

<sup>5</sup>Lead Contact

\*Correspondence: [arthur.konnerth@tum.de](mailto:arthur.konnerth@tum.de)

<https://doi.org/10.1016/j.celrep.2019.04.007>

## SUMMARY

The cerebral cortex is organized in vertical columns that contain neurons with similar functions. The cellular micro-architecture of such columns is an essential determinant of brain dynamics and cortical information processing. However, a detailed understanding of columns is incomplete, even in the best studied cortical regions, and mostly restricted to the upper cortical layers. Here, we developed a two-photon  $\text{Ca}^{2+}$ -imaging-based method for the serial functional mapping of all pyramidal layers of the mouse primary auditory cortex at single-neuron resolution in individual animals. We demonstrate that the best frequency-responsive neurons are organized in all-layers-crossing narrow columns, with fuzzy boundaries and a bandwidth of about one octave. This micro-architecture is, in many ways, different from what has been reported before, indicating the region and stimulus specificity of functional cortical columns *in vivo*.

## INTRODUCTION

Vertical columns of neurons with similar functions are widely considered to be a hallmark of cortical organization in the mammalian brain (Mountcastle, 1997; Rakic, 2008). Early evidence for such cortical columns was based on electrophysiological recordings, first in the somato-sensory cortex (Mountcastle et al., 1955) followed by recordings in other regions, for example, in the primary visual (Hubel and Wiesel, 1968) and the auditory cortex (Abeles and Goldstein, 1970; Atencio and Schreiner, 2010; Merzenich et al., 1975; Oonishi and Katsuki, 1965). However, microelectrode recordings are biased toward the detection of firing neurons and blind to inactive neurons. Furthermore, such recordings provide only a sparse sample of the neurons in a column with imprecise neuronal localization and are not suitable to accurately resolve columnar boundaries. These limitations can be overcome by optical imaging with single-cell resolution (Stosiek et al., 2003). For example, Ohki et al. (2005)

used two-photon calcium imaging for the analysis of the columnar boundaries in supragranular layers of area 18 in the cat visual cortex and found that “neurons with opposite preferences for stimulus direction were segregated [...] with columnar borders one to two cells wide.” Similarly, in the mouse barrel cortex, *in vivo* two-photon imaging recordings demonstrated segregated single whisker-specific neuronal domains in layer 4 (L4), with sharp cellular borders between neighboring “barrels” (Jia et al., 2014). However, functional *in vivo* imaging studies that provide an integral picture of all cortical layers are largely missing. An elegant study by Peron et al. (2015) reported the functional properties of neurons in the somato-sensory cortex in individual mice in layers 2/3 (L2/3) and 5 (L5), but L4 and layer 6 (L6) were missing. Another study investigating cortical microarchitecture identified mini- and microcolumns in larger sections of L2/3, L4, and L5 neurons in the mouse visual cortex (Kondo et al., 2016). Finally, a more complete but invasive approach involved the use of cortically implanted microprisms and obtained a side view of all cortical layers in the same animal (Andermann et al., 2013). However, this approach disrupts intracortical and afferent axons, potentially modifying neuronal activity patterns. Here, we overcame these limitations by developing an imaging approach that allows access to all cortical layers in the same microcolumn without using a prism. We constructed an integral functional map of neurons in a cortical column of the mouse primary auditory cortex, in which we included “irregular” neurons that were spontaneously active but not reliably responsive to sensory stimulation, as well as “silent” neurons that were entirely inactive during the period of recording.

## RESULTS

For a wide-ranging cellular analysis of all cortical layers of the mouse primary auditory cortex *in vivo* (A1), we combined “conventional” (Stosiek et al., 2003) and deep two-photon  $\text{Ca}^{2+}$  imaging of neuronal circuits (Tischbirek et al., 2015) with flavoprotein autofluorescence imaging of the brain surface (Takahashi et al., 2006) in lightly anesthetized and awake animals. In a sequential imaging approach, we first used autofluorescence brain surface imaging to functionally identify A1 through the intact skull (Figure 1A). The center points of the autofluorescence changes



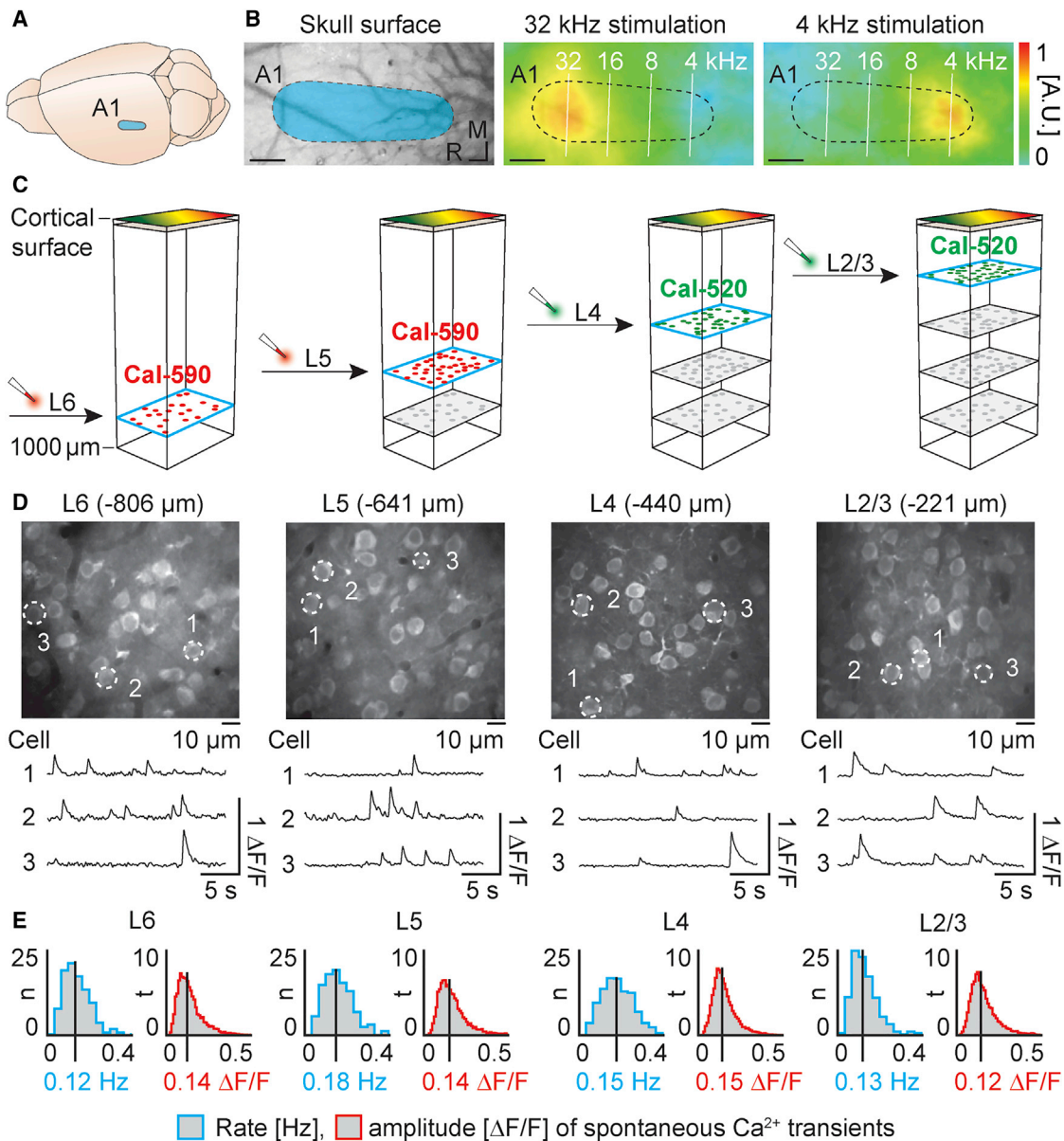


**Figure 1. A Functional 3D Mapping Approach of a Cortical Column with Single-Cell Resolution**

(A) Schematic of the adult mouse brain. Location of the primary auditory cortex (A1) is indicated by the blue patch.

(B) Left: skull overlying the left auditory cortex. A1 is indicated by the blue patch. Right: brain surface imaging examples showing the autofluorescence response during pure-tone stimulation with 32 kHz and 4 kHz. Black dotted lines indicate A1 boundary. Scale bars: 200  $\mu\text{m}$ .

(C) Illustration of the sequential labeling and recording procedure to measure activity from neurons in all cortical layers.

(D) *In vivo* two-photon imaging of neurons stained with Cal-590 AM from cortical L2/3, L4, L5, and L6 in A1 with light MMF anesthesia. Recording depth below the cortical surface is indicated above the images (average of 2,480 frames at 80 Hz). Examples of spontaneous  $\text{Ca}^{2+}$  transients correspond to the cells indicated by white dotted lines.

(E) Rate of spontaneous  $\text{Ca}^{2+}$  transients (blue) and corresponding  $\Delta F/F$  values (red) for each cortical layer in A1. n, percentage of cells. Absolute cell number: L2/3, 385; L4, 161; L5, 502; and L6, 496. t, percentage of transients. Absolute number of transients: L2/3, 7,014; L4, 6,347; L5, 15,304; and L6, 8,439.

evoked by 4- and 32-kHz pure-tone stimulation (Figure 1B) were used to define the tonotopic axis of A1. The tonotopic axis was used to target a location for two-photon  $\text{Ca}^{2+}$  imaging. In an attempt to maximally reduce the out-of-focus fluorescence from overlying labeled cortical structures (Birkner et al., 2017;

Helmchen and Denk, 2005), we developed a “serial bottom first” two-photon imaging approach in which we started the two-photon  $\text{Ca}^{2+}$  imaging recordings with the deepest cortical layer (Figure 1C). Recordings of neuronal activity in depths up to 900  $\mu\text{m}$  below the cortical surface were possible with the use

of Cal-590 AM, a red-shifted  $\text{Ca}^{2+}$ -sensitive fluorescent dye (Tischbirek et al., 2015). Alexa Fluor 680 was added to the staining solution to optically control and restrict the volume of the dye staining (diameter less than 200–250  $\mu\text{m}$ ), which is essential for avoiding out-of-focus fluorescence (Birkner et al., 2017). After recording neuronal activity in L6, L5 was also stained with Cal-590 AM to record neuronal activity. In line with previous multiunit electrode recordings (Christianson et al., 2011), we observed a somewhat higher rate of spontaneous  $\text{Ca}^{2+}$  transients in L5 (Figure 1D; Kruskal-Wallis test,  $\chi^2 = 164$ ,  $p = 2.3 \times 10^{-35}$ ; Mann-Whitney U test between L5 and the other layers with Bonferroni-Holm correction,  $p < 0.01$ ). Since diffusion of Cal-590 into the apical dendrites of L5 and L6 neurons causes an increase in background fluorescence in the upper cortical layers at the corresponding emission wavelength, we switched to the green  $\text{Ca}^{2+}$  dye Cal-520 AM (Tada et al., 2014) to map the somatic neuronal activity in L4 and, in a next step, L2/3 (Figures 1C and 1D). In control experiments, we compared recordings obtained with Cal-520 AM and Cal-590 AM staining, respectively, and found no significant difference for the rate of spontaneous  $\text{Ca}^{2+}$  transients in L2/3 with both dyes (Mann-Whitney U test,  $p = 0.26$ ;  $n = 7$  animals). A comparison of the spontaneous activity in the various cortical layers revealed comparable amplitude distributions of  $\text{Ca}^{2+}$  transients throughout all cortical depths and the somewhat higher rates of  $\text{Ca}^{2+}$  transients in L5 (Figure 1E). The results demonstrate the feasibility of our “serial bottom first” approach of sequential population  $\text{Ca}^{2+}$  recordings of neuronal activity from a column-like cortical structure with single-cell resolution in individual animals. Complete recordings in individual animals are necessary, because they allow the most precise top-down alignment of corresponding cortical fields and, moreover, minimize errors associated with inter-animal anatomical variability (Kondo et al., 2016).

For the functional mapping of mouse A1, we recorded sound-evoked  $\text{Ca}^{2+}$  transients and determined, for individual neurons, the frequency response area (FRA; Figure S1) and calculated the best frequency (BF) (Guo et al., 2012). For this purpose, we recorded, for each neuron in our study ( $n = 4,856$  in 56 mice), 8–10 trials for every condition (frequency range, 2–45.3 kHz; 5 attenuation levels), summing up to a total of 750–900  $\text{Ca}^{2+}$  transients per neuron in response to pure-tone stimulation. We used 19 stimulus frequencies that were separated by a quarter octave, in line with the relatively wide critical bands of the mouse (Ehret, 1976) and the broad tuning of neurons in the mouse auditory cortex (Guo et al., 2012; Linden et al., 2003). Figures 2A–2C illustrate representative recordings obtained in an L2/3 neuron. We demonstrate that sound-evoked recordings of neuronal BF patterns obtained in alert animals (Figure 2B) are highly similar to those recorded in conditions of light medetomidine, midazolam, and fentanyl (MMF) anesthesia (Figures 2C and S2), which is consistent with previously reported findings (Guo et al., 2012). In order to avoid the need for movement correction, we included here only recordings obtained under light MMF anesthesia. The use of functional imaging allowed us to determine under both conditions the fractions of “irregular” and “silent” neurons. We define “irregular” neurons as spontaneously active neurons with highly variable responses to sound stimulation, largely corresponding to the class of neurons described by Guo et al. (2012)

(see STAR Methods for details). “Silent” neurons were defined as those neurons that were completely inactive during our recording time (>30 min). Figure 2D shows that MMF anesthesia had little impact on the fractions of frequency-tuned, “irregular” and “silent” neurons, with small variability between individual preparations (Wilcoxon signed rank test for tuned neurons,  $p = 0.125$ ; for “silent” neurons,  $p = 0.3750$  after Bonferroni correction).

Next, we attempted to determine the degree of tonotopy in all cortical pyramidal layers of A1 in relation to the surface map. Previous optical recordings were restricted to the upper L2/3 and L4 (Bandyopadhyay et al., 2010; Issa et al., 2014; Li et al., 2017; Rothschild et al., 2010; Winkowski and Kanold, 2013). Extracellular electrical recordings also included deeper layers (Guo et al., 2012), but specific data with sufficient spatial resolution to image the responses of individual cells in L5 and L6 are still missing. Figure 2F summarizes systematic two-photon imaging experiments in which we determined the median BF of all neurons within an imaging frame and related the resulting frame BF to the cortical surface map. The frame size was 200  $\mu\text{m} \times 130 \mu\text{m}$ , and each frame contained about 30–40 cell bodies (used to calculate the median BF). In each layer, we recorded imaging frames in multiple animals, which covered >90% of the distance along the tonotopic axis. In L2/3, recordings from the various trials were obtained at different depths of a large core region of the layer (ranging between –195  $\mu\text{m}$  and –335  $\mu\text{m}$ , with a mean spacing between imaging planes of about 9  $\mu\text{m}$  along the z axis), L4 depths ranged from 380  $\mu\text{m}$  to 466  $\mu\text{m}$  (5.5- $\mu\text{m}$  spacing), L5 depths ranged from 571  $\mu\text{m}$  to 648  $\mu\text{m}$  (8.5- $\mu\text{m}$  spacing), and L6 depths ranged from 778  $\mu\text{m}$  to 869  $\mu\text{m}$  (9- $\mu\text{m}$  spacing). The results reveal gradients of median BF that were similar in all cortical layers (Figure 2F, left column). These coarse, layer-specific maps, which are preserved from the cortical surface down to L5 and L6 (Figure 2F, right column), strongly support the notion of a columnar organization of A1 along the entire tonotopic axis.

What is the neuronal micro-architecture of such vertically organized columns? Direct experimental tests for the identification of functional columns are challenging, as A1 is located laterally in the mouse brain (Figure 1A), and the brain curvature makes an accurate vertical alignment across different cortical layers difficult. To overcome this limitation, we established an approach using the apical dendrites of L5 pyramidal neurons, which extend their tips to the cortical surface, as anatomical markers for the columnar axis. For this purpose, we labeled, in individual experiments, up to 20 L5 pyramidal neurons with the fluorescent dye Alexa Fluor 680 by single-cell electroporation (Figure 3A) just before  $\text{Ca}^{2+}$  imaging. We used the dendrites, seen in all imaging fields within the same column, to align L2/3 and L4 with the corresponding regions of L5 and extended the alignment to L6 by extrapolating the L5 apical dendrites. Figures 3B–3D illustrate results obtained entirely in an individual animal and demonstrates that, within an imaging field, neuronal BFs were variable but that the variability spanned only over a narrow range among all stimulation frequencies. The variability of BFs within an imaging field was similar in all layers (Figure 3C; Bartlett’s statistic for difference of variability between layers = 4.65,  $p = 0.199$ ). Furthermore, the example experiment

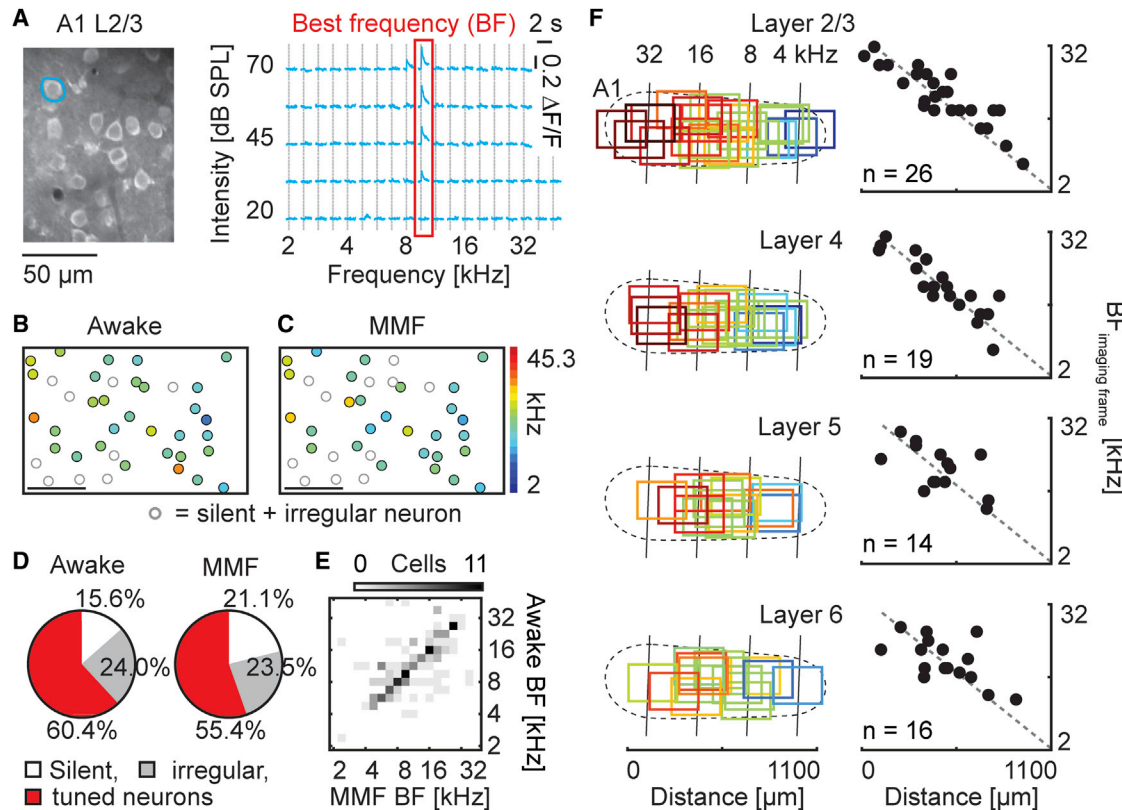


**Figure 2. Tonotopy of Neuronal BF Responses in All Pyramidal Layers**

(A) Left: two-photon image (average of 2,480 frames) of the focal plane used to image L2/3 neurons in A1. Right: sound-evoked  $\text{Ca}^{2+}$  transients corresponding to pure-tone stimulation (average of 7–10 trials). Responses for the blue region of interest indicated in the left panel are indicated. Red outline marks the best-frequency (BF) response.

(B and C) BF map of A1 L2/3 neurons in a non-anesthetized mouse. Color code is on the right side of (C). Scale bar: 50  $\mu\text{m}$ . Same animal as in (B) were treated with MMF (C). Same conventions were used as in (B).

(D) Pie charts showing the percentage of responsive neurons to pure-tone stimulation in awake and MMF-anesthetized mice ( $n = 5$  animals; see STAR Methods for the definitions of “silent” and “irregular” neurons).

(E) Graph showing the correlation of the BF responses of individual neurons during wakefulness and anesthesia (Pearson’s correlation coefficient,  $R = 0.668$ ,  $p = 4.83 \times 10^{-23}$ ). Data shown here were recorded in  $n = 5$  animals.

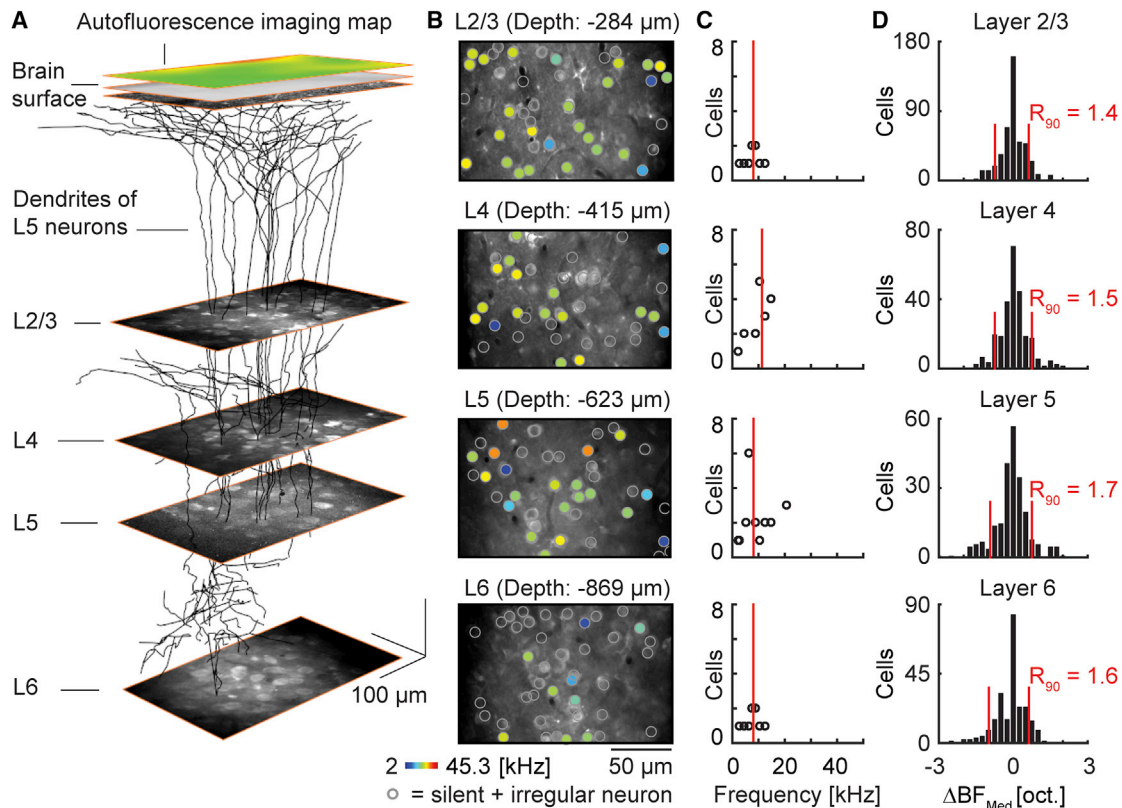
(F) Left: schematic illustrating the recording locations of individual fields of view in A1. Outlines are color coded according to median BF response in the respective fields of view (same color scale as in C). Black dotted lines indicate the approximate location of A1. Right: scatterplots showing the correlation between the cellular  $\text{BF}_{\text{median}}$  values measured in the fields of view with two-photon imaging and the corresponding extrapolated brain surface frequencies determined by autofluorescence imaging.

demonstrates that frequency responses are vertically preserved at the level of individual neurons in all cortical layers.

Measurements in multiple mice (L2/3,  $n = 26$ ; L4,  $n = 18$ ; L5,  $n = 15$ ; and L6,  $n = 18$  animals) showed that the BF variability in all layers within an analysis window of  $200 \mu\text{m} \times 130 \mu\text{m}$  was smaller (mean  $R_{90}$  of all layers = 1.55 octaves  $\pm$  0.13 octaves) than reported in previous studies (Bandyopadhyay et al., 2010; Winkowski and Kanold, 2013) (Figure 3D; see Figure S3 for additional FRA parameters). Overall, these results show an intermediate BF variability relative to that in previous reports. The narrow-band BF variability as reported here was substantially larger than that suggested by Issa et al. (2014) and by the L4 recordings of Winkowski and Kanold (2013) but lower than the variability implied from the L2/3 recordings of Bandyopadhyay et al. (2010), Rothschild et al. (2010), and Winkowski and Kanold

(2013). Our results are roughly consistent with previously reported electrophysiological data (Guo et al., 2012), with the added advantage of the dense coverage of neurons within each imaging field.

A readily observable feature in each layer corresponding to a column-like bundle of L5 apical dendrites (as shown in Figure 3A) is the amount of “irregular” or “silent” neurons (gray symbols in Figure 4A). Indeed, we observed a similar percentage of neurons responding to auditory stimulation in all cortical layers (Pearson’s  $\chi^2$  test,  $\chi^2 = 78.0$ ,  $p = 0.294$ , Figure 4B), and more than half of the neurons were “irregular” or “silent” in all layers. In line with this finding, we found a skewed distribution of response strengths within each layer (Figure S4A), with only a relatively small fraction of neurons responding strongly to pure-tone stimulation. Such distributions are in line with the notion of sparse representation

**Figure 3. Vertical Organization of the Local Cortical Heterogeneity of BFs**

- (A) Reconstruction of an imaging region with dendrites of L5 pyramidal neurons filled by single-cell electroporation for the precise alignment of individual imaging regions in all cortical layers.
- (B) Two-photon image (average of 2,480 frames) of the focal plane used to image L2/3 neurons in A1. Overlaid circles mark regions of interest, which are color coded according to the BF. Open gray circles correspond to “silent” and “irregular” neurons.
- (C) Histogram of the BFs of individual neurons within the field of view shown in (B).
- (D) Histogram of the difference of the BF of individual neurons from the median frequency in the respective imaging fields of view.  $R_{90}$ , the 90% range of the histogram in octaves. For L2/3, n = 501 cells; for L4, n = 430 cells; for L5, n = 357 cells; and for L6, n = 412 cells.

of the pure-tone stimulation (Hromádka et al., 2008) and were observed across all cortical layers. We conclude that inactive and silent cells make up a significant portion of the micro-architecture of vertically organized columns. For the neurons that actually had significant responses to sensory stimulation, we found that neurons with higher BFs (indicated in red) tended to cluster on the anterior edge of the imaging field, while those with lower BFs (indicated in green) were more abundant on the posterior edge. The separation between neurons with similar BFs was by no means abrupt. Distances between neurons with the same BF could exceed 400 μm (Figure S4B). In view of the local bandwidth of about one octave at any given spot in A1 (Figure 4A), we wondered about the minimal distance along the tonotopic axis at which a significant BF difference becomes discernable. To address this issue, we analyzed the BF distribution within rectangular analysis windows (width of 30–90 μm) with their long axis orthogonal to the tonotopic gradient (Figure 4C). By systematically changing the distance between the midpoints of the analysis windows, we determined the minimal distance at which the median BFs became significantly different. Figure 4D illustrates the

analysis of a recording in L6—the most challenging experimental condition—and shows that, for this imaging field, the median BFs were significantly different at a distance of 100 μm (Mann-Whitney U test, p values after Bonferroni-Holm correction: 1 versus 2: 0.124; 1 versus 3: 0.0396; and 2 versus 3: 0.103). Across all experiments performed in L2/3, L4, L5, and L6, the minimal distances for detecting significant differences (L2/3, 69 μm, n = 20; L4, 72 μm, n = 17; L5, 75 μm, n = 13; and L6, 58 μm, n = 11) were quite similar to each other (Figure 4E, Kruskal-Wallis test for difference between layers:  $\chi^2 = 2.79$ , p = 0.425; see also Figure S5). Thus, although the data did not reveal in A1 clearly defined functional columns with the same BFs having crisp transitions between them, vertical electrode penetrations spaced at intervals of 80–90 μm would report significantly different median BFs and would be interpreted as functional “columns.” Our imaging experiments provide a cellular explanation for the early electrical recordings of Abeles and Goldstein (1970), who suggested that “if there are such columns in the auditory cortex, they are small (ca. 100 μm diameter) and at the limit of the resolution of the technique employed.”

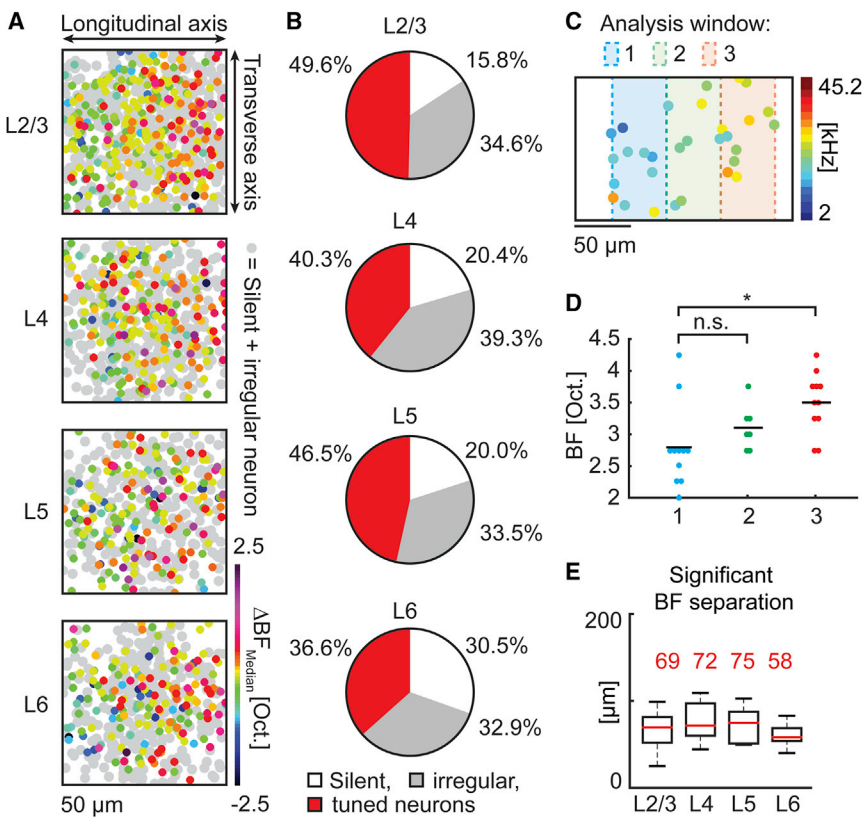


**Figure 4. Dimension and Functional Micro-structure of Cortical Columns in A1**

(A) BF maps of each cortical layer. Each circle represents one neuron. Difference from median is shown to align multiple experiments (L2/3,  $n = 20$ ; L4,  $n = 17$ ; L5,  $n = 13$ ; and L6,  $n = 11$  animals). The longitudinal axis is defined as the axis along which the maximum BF gradient was observed in each experiment. Color scale is indicated on the bottom right. Neurons without frequency tuning are indicated by gray circles.

(B) Pie charts showing the percentage of neurons responsive to pure-tone stimulation in the primary auditory cortex (see STAR Methods for the definition of “silent” and “irregular” neurons).

(C) Example region showing the BFs of individual neurons in L6 of A1. Three rectangular analysis windows ( $50 \times 130 \mu\text{m}$ ) are indicated in blue, green, and red. The windows are shifted along the tonotopic gradient by  $50 \mu\text{m}$ .

(D) BFs of individual neurons within the analysis windows indicated in (E) plotted with blue (1), green (2), and red (3) symbols, respectively. Black lines indicate the median BF for the respective analysis windows. Significance of  $p$  values (Mann-Whitney U test with Holm-Bonferroni method, \* $p < 0.05$ ; exact values in text) is indicated above the graph. n.s., not significant.

(E) Distance along the longitudinal axis to reach a significant BF change. Red numbers indicate median distance in microns measured for the respective layers. Same dataset as shown in (A).

## DISCUSSION

In conclusion, our results provide two-photon  $\text{Ca}^{2+}$ -imaging-based recordings of functional columns *in vivo* down to L6 in individual animals. The “serial bottom first” approach of two-photon imaging involved the combined use of red-shifted (Cal-590 AM) and green (Cal-520 AM) synthetic fluorescence  $\text{Ca}^{2+}$  indicators. The acute staining of the different cortical layers, sequentially from the deepest L6 up to L2/3, was essential for maximally avoiding the out-of-focus fluorescence from overlying labeled cortical structures (Birkner et al., 2017; Helmchen and Denk, 2005). The use of genetically encoded  $\text{Ca}^{2+}$  indicators (GECIs) would have the benefit of larger neuronal responses and the possibility to discriminate between neuron and interneuron subtypes, which might contribute to the response variability observed within different cell layers. However, GECIs would be limited in terms of response kinetics (Chen et al., 2013), difficulties in efficiently staining L4 (e.g., Peron et al., 2015), and the prolonged waiting periods between the sequential expression of the GECIs in different cortical layers.

The 3D map of an A1 cortical column provides an integral account of active and non-active neurons throughout all pyramidal neuron-containing L2/3, L4, L5, and L6, avoiding the inherent bias of electrical recordings in which only spiking cells can be detected. In view of the highly preserved tonotopy observed with various approaches in different species, including rodents (Guo et al., 2012; Hackett et al., 2011; Stiebler et al., 1997), carnivores

(Bizley et al., 2005; Merzenich et al., 1975), and non-human primates (Merzenich and Brugge, 1973), the micro-architecture revealed in the present study is likely to reflect a basic principle of organization in the mammalian brain. So far, the best investigated cortical micro-architectures on the cellular level *in vivo* are probably those of the primary visual (Ohki et al., 2005, 2006) and the somatosensory barrel cortex in rodents (Jia et al., 2014; Varga et al., 2011). The cellular understanding in those regions is restricted to the granular and supragranular layers, with limited information on L5 and L6. In the mouse barrel cortex, for example, *in vivo* two-photon imaging recordings indicated a strict whisker-specific functional organization in L4 (Jia et al., 2014), which becomes promiscuous in L2/3 with substantial inputs from the surround whiskers (Varga et al., 2011). In the visual cortex, the functional maps are species specific, with a pronounced columnar organization of direction-selective neurons, for example, in cats and non-human primates (Hubel and Wiesel, 1968; Mountcastle et al., 1955).

Even for the same sensory modality, different types of sensory stimulation may highlight different patterns of micro-architectural organization in given sensory cortical regions (Kondo et al., 2016; Niell and Stryker, 2008), making simple categorizations and comparisons across various modalities difficult. Nonetheless, our present study indicates that the auditory cortex has some distinctive features that were not encountered and/or reported in earlier studies. These include the fuzzy boundary, the remarkable local heterogeneity, and the sparse coding

throughout all layers. More specifically, in all layers, we found that neurons with the same BFs, although generally clustered at well-defined locations along the tonotopic axis, could be spatially distributed over distances of up to a few hundreds of microns. This spatially organized mix of heterogeneity at the micro-scale and the preservation of more stable response patterns at a larger scale may reflect developmental and learning-dependent wiring rules in the auditory cortex. Our study provides a framework that allows an in-depth investigation for such wiring and response rules in the auditory and also in other cortical areas.

## STAR★METHODS

Detailed methods are provided in the online version of this paper and include the following:

- KEY RESOURCES TABLE
- CONTACT FOR REAGENT AND RESOURCE SHARING
- EXPERIMENTAL MODEL AND SUBJECT DETAILS
- METHOD DETAILS
  - Surgery
  - Autofluorescence imaging
  - Two-photon imaging
  - Dye loading
  - Electroporation
  - Auditory stimulation
  - Electromyographic (EMG) recordings and analysis
- QUANTIFICATION AND STATISTICAL ANALYSIS
  - Autofluorescence imaging data analysis
  - Two-photon imaging data processing

## SUPPLEMENTAL INFORMATION

Supplemental Information can be found online at <https://doi.org/10.1016/j.celrep.2019.04.007>.

## ACKNOWLEDGMENTS

This work was supported by grants from the Deutsche Forschungsgemeinschaft (SFB 870) and European Research Council Advanced Grants to A.K. and I.N., respectively. A.K. is a Hertie Senior Professor for Neuroscience.

## AUTHOR CONTRIBUTIONS

C.H.T., T.N., I.N., and A.K. designed research. C.H.T., T.N., and A.K. performed research. M.T. and A.B. gave support with imaging hard- and software. C.H.T., T.N., I.N., and A.K. analyzed the data and wrote the manuscript.

## DECLARATION OF INTERESTS

The authors declare no competing financial interests.

Received: December 3, 2018

Revised: February 26, 2019

Accepted: March 29, 2019

Published: April 30, 2019

## REFERENCES

- Abeles, M., and Goldstein, M.H., Jr. (1970). Functional architecture in cat primary auditory cortex: columnar organization and organization according to depth. *J. Neurophysiol.* **33**, 172–187.
- Andermann, M.L., Gilfoy, N.B., Goldey, G.J., Sachdev, R.N., Wölfel, M., McCormick, D.A., Reid, R.C., and Levine, M.J. (2013). Chronic cellular imaging of entire cortical columns in awake mice using microprisms. *Neuron* **80**, 900–913.
- Anderson, L.A., Christianson, G.B., and Linden, J.F. (2009). Mouse auditory cortex differs from visual and somatosensory cortices in the laminar distribution of cytochrome oxidase and acetylcholinesterase. *Brain Res.* **1252**, 130–142.
- Atencio, C.A., and Schreiner, C.E. (2010). Laminar diversity of dynamic sound processing in cat primary auditory cortex. *J. Neurophysiol.* **103**, 192–205.
- Bandyopadhyay, S., Shamma, S.A., and Kanold, P.O. (2010). Dichotomy of functional organization in the mouse auditory cortex. *Nat. Neurosci.* **13**, 361–368.
- Birkner, A., Tischbirek, C.H., and Konnerth, A. (2017). Improved deep two-photon calcium imaging in vivo. *Cell Calcium* **64**, 29–35.
- Bizley, J.K., Nodal, F.R., Nelken, I., and King, A.J. (2005). Functional organization of ferret auditory cortex. *Cereb. Cortex* **15**, 1637–1653.
- Chen, T.W., Wardill, T.J., Sun, Y., Pulver, S.R., Renninger, S.L., Baohan, A., Schreiter, E.R., Kerr, R.A., Orger, M.B., Jayaraman, V., et al. (2013). Ultrasensitive fluorescent proteins for imaging neuronal activity. *Nature* **499**, 295–300.
- Christianson, G.B., Sahani, M., and Linden, J.F. (2011). Depth-dependent temporal response properties in core auditory cortex. *J. Neurosci.* **31**, 12837–12848.
- Ehret, G. (1976). Critical bands and filter characteristics in the ear of the house-mouse (*Mus musculus*). *Biol. Cybern.* **24**, 35–42.
- Guo, W., Chambers, A.R., Darrow, K.N., Hancock, K.E., Shinn-Cunningham, B.G., and Polley, D.B. (2012). Robustness of cortical topography across fields, laminae, anesthetic states, and neurophysiological signal types. *J. Neurosci.* **32**, 9159–9172.
- Hackett, T.A., Barkat, T.R., O'Brien, B.M., Hensch, T.K., and Polley, D.B. (2011). Linking topography to tonotopy in the mouse auditory thalamocortical circuit. *J. Neurosci.* **31**, 2983–2995.
- Hagihara, K.M., Murakami, T., Yoshida, T., Tagawa, Y., and Ohki, K. (2015). Neuronal activity is not required for the initial formation and maturation of visual selectivity. *Nat. Neurosci.* **18**, 1780–1788.
- Helmchen, F., and Denk, W. (2005). Deep tissue two-photon microscopy. *Nat. Methods* **2**, 932–940.
- Hromádka, T., Deweese, M.R., and Zador, A.M. (2008). Sparse representation of sounds in the unanesthetized auditory cortex. *PLoS Biol.* **6**, e16.
- Hubel, D.H., and Wiesel, T.N. (1968). Receptive fields and functional architecture of monkey striate cortex. *J. Physiol.* **195**, 215–243.
- Issa, J.B., Haeffele, B.D., Agarwal, A., Bergles, D.E., Young, E.D., and Yue, D.T. (2014). Multiscale optical Ca<sup>2+</sup> imaging of tonal organization in mouse auditory cortex. *Neuron* **83**, 944–959.
- Jia, H., Varga, Z., Sakmann, B., and Konnerth, A. (2014). Linear integration of spine Ca<sup>2+</sup> signals in layer 4 cortical neurons in vivo. *Proc. Natl. Acad. Sci. USA* **111**, 9277–9282.
- Kerlin, A.M., Andermann, M.L., Berezovskii, V.K., and Reid, R.C. (2010). Broadly tuned response properties of diverse inhibitory neuron subtypes in mouse visual cortex. *Neuron* **67**, 858–871.
- Kondo, S., Yoshida, T., and Ohki, K. (2016). Mixed functional microarchitectures for orientation selectivity in the mouse primary visual cortex. *Nat. Commun.* **7**, 13210.
- Li, J., Zhang, J., Wang, M., Pan, J., Chen, X., and Liao, X. (2017). Functional imaging of neuronal activity of auditory cortex by using Cal-520 in anesthetized and awake mice. *Biomed. Opt. Express* **8**, 2599–2610.
- Linden, J.F., Liu, R.C., Sahani, M., Schreiner, C.E., and Merzenich, M.M. (2003). Spectrotemporal structure of receptive fields in areas AI and AAF of mouse auditory cortex. *J. Neurophysiol.* **90**, 2660–2675.
- Longair, M.H., Baker, D.A., and Armstrong, J.D. (2011). Simple Neurite Tracer: open source software for reconstruction, visualization and analysis of neuronal processes. *Bioinformatics* **27**, 2453–2454.

- Merzenich, M.M., and Brugge, J.F. (1973). Representation of the cochlear partition of the superior temporal plane of the macaque monkey. *Brain Res.* **50**, 275–296.
- Merzenich, M.M., Knight, P.L., and Roth, G.L. (1975). Representation of cochlea within primary auditory cortex in the cat. *J. Neurophysiol.* **38**, 231–249.
- Moshitch, D., Las, L., Ulanovsky, N., Bar-Yosef, O., and Nelken, I. (2006). Responses of neurons in primary auditory cortex (A1) to pure tones in the halothane-anesthetized cat. *J. Neurophysiol.* **95**, 3756–3769.
- Mountcastle, V.B. (1997). The columnar organization of the neocortex. *Brain* **120**, 701–722.
- Mountcastle, V., Berman, A., and Davies, P. (1955). Topographic organization and modality representation in first somatic area of cat's cerebral cortex by method of single unit analysis. *Am. J. Physiol.* **183**, 646.
- Niell, C.M., and Stryker, M.P. (2008). Highly selective receptive fields in mouse visual cortex. *J. Neurosci.* **28**, 7520–7536.
- Noda, T., and Takahashi, H. (2015). Anesthetic effects of isoflurane on the tonotopic map and neuronal population activity in the rat auditory cortex. *Eur. J. Neurosci.* **42**, 2298–2311.
- Ohki, K., Chung, S., Ch'ng, Y.H., Kara, P., and Reid, R.C. (2005). Functional imaging with cellular resolution reveals precise micro-architecture in visual cortex. *Nature* **433**, 597–603.
- Ohki, K., Chung, S., Kara, P., Hübener, M., Bonhoeffer, T., and Reid, R.C. (2006). Highly ordered arrangement of single neurons in orientation pinwheels. *Nature* **442**, 925–928.
- Oonishi, S., and Katsuki, Y. (1965). Functional organization and integrative mechanism on the auditory cortex of the cat. *Jpn. J. Physiol.* **15**, 342–365.
- Peron, S.P., Freeman, J., Iyer, V., Guo, C., and Svoboda, K. (2015). A cellular resolution map of barrel cortex activity during tactile behavior. *Neuron* **86**, 783–799.
- Rakic, P. (2008). Confusing cortical columns. *Proc. Natl. Acad. Sci. USA* **105**, 12099–12100.
- Rothschild, G., Nelken, I., and Mizrahi, A. (2010). Functional organization and population dynamics in the mouse primary auditory cortex. *Nat. Neurosci.* **13**, 353–360.
- Schreiner, C.E., and Sutter, M.L. (1992). Topography of excitatory bandwidth in cat primary auditory cortex: single-neuron versus multiple-neuron recordings. *J. Neurophysiol.* **68**, 1487–1502.
- Stiebler, I., Neulist, R., Fichtel, I., and Ehret, G. (1997). The auditory cortex of the house mouse: left-right differences, tonotopic organization and quantitative analysis of frequency representation. *J. Comp. Physiol. A Neuroethol. Sens. Neural Behav. Physiol.* **181**, 559–571.
- Stosiek, C., Garaschuk, O., Holthoff, K., and Konnerth, A. (2003). In vivo two-photon calcium imaging of neuronal networks. *Proc. Natl. Acad. Sci. USA* **100**, 7319–7324.
- Tada, M., Takeuchi, A., Hashizume, M., Kitamura, K., and Kano, M. (2014). A highly sensitive fluorescent indicator dye for calcium imaging of neural activity in vitro and in vivo. *Eur. J. Neurosci.* **39**, 1720–1728.
- Takahashi, K., Hishida, R., Kubota, Y., Kudoh, M., Takahashi, S., and Shibuki, K. (2006). Transcranial fluorescence imaging of auditory cortical plasticity regulated by acoustic environments in mice. *Eur. J. Neurosci.* **23**, 1365–1376.
- Tischbirek, C., Birkner, A., Jia, H., Sakmann, B., and Konnerth, A. (2015). Deep two-photon brain imaging with a red-shifted fluorometric Ca<sup>2+</sup> indicator. *Proc. Natl. Acad. Sci. USA* **112**, 11377–11382.
- Varga, Z., Jia, H., Sakmann, B., and Konnerth, A. (2011). Dendritic coding of multiple sensory inputs in single cortical neurons in vivo. *Proc. Natl. Acad. Sci. USA* **108**, 15420–15425.
- Winkowski, D.E., and Kanold, P.O. (2013). Laminar transformation of frequency organization in auditory cortex. *J. Neurosci.* **33**, 1498–1508.

**STAR★METHODS****KEY RESOURCES TABLE**

REAGENT or RESOURCE	SOURCE	IDENTIFIER
Chemicals, Peptides, and Recombinant Proteins		
Cal-520 AM	AAT Bioquest, Sunnyvale	21130
Cal-590 AM	AAT Bioquest, Sunnyvale	20511
Alexa 594	Life Technologies, Darmstadt	A10438
Alexa 680	Life Technologies, Darmstadt	A20344
Agarose	Life Technologies, Darmstadt	15510-027
Xylocain	Aspen Pharma (WDT), Garbsen	778805
Medetomidine	Orion Pharma (WDT), Garbsen	20020
Midazolam	ratiopharm (WDT), Garbsen	22920
Fentanyl	Jannsen (WDT), Garbsen	22567
Metamizole	bela-pharm, Hamburg	799285
NaCl	Merck, Darmstadt	1.06404.1000
KCl	Merck, Darmstadt	1.04936.1000
NaH <sub>2</sub> PO <sub>4</sub>	Sigma-Aldrich, Steinheim	S9638
NaHCO <sub>3</sub>	Merck, Darmstadt	1.06329.1000
CaCl <sub>2</sub>	Applichem, Darmstadt	131232.1210
MgCl <sub>2</sub>	Merck, Darmstadt	1.05833.0250
Glucose	Merck, Darmstadt	1.08342.1000
DMSO	Sigma-Aldrich, Steinheim	D8779
pluronic-F127	Sigma-Aldrich, Steinheim	P2443
HEPES	Sigma-Aldrich, Steinheim	H3375
K-Gluconate	Sigma-Aldrich, Steinheim	P1847
Na <sub>2</sub> Phosphocreatine	Sigma-Aldrich, Steinheim	P7936
Mg-ATP	Sigma-Aldrich, Steinheim	P7936
Na-GTP	Sigma-Aldrich, Steinheim	A9187
Other		
Borosilicate glass capillaries	Hilgenberg GmbH	1807516
470 nm LED	Thorlabs	M470L2-C1
CMOS camera Andor Zyla 4.2 Plus	Andor	ZYLA-4.2P-USB3
Beam expander	Thorlabs	BE02M-B
Two-photon microscope dichroic mirror	AHF Analysentechnik	F73-705
Hybrid photo detector	Hamamatsu	R7110U-40
Electrostatic loudspeaker	Tucker Davis Technologies	ED1

**CONTACT FOR REAGENT AND RESOURCE SHARING**

Further information and requests for resources and reagents should be directed to and will be fulfilled by the Lead Contact, Arthur Konnerth ([arthur.konnerth@tum.de](mailto:arthur.konnerth@tum.de)).

**EXPERIMENTAL MODEL AND SUBJECT DETAILS**

All experimental procedures were performed in accordance with institutional animal welfare guidelines and were approved by the state government of Bavaria, Germany. C57BL/6 mice (postnatal days 30–37) of both sexes were used.

## METHOD DETAILS

### Surgery

Initial anesthesia during surgery was induced with isoflurane 1.5% vol/vol in O<sub>2</sub> and continued with MMF (in mg/kg body weight: medetomidine 0.05, midazolam 0.5, fentanyl: 0.005) for the recording. Biomonitoring was applied, and the mouse was kept at 37.5°C with a heating pad. After local anesthesia (2% xylocaine) and analgesia (metamizole, 200 mg/kg) was applied, the skull was exposed. A custom-made recording chamber was attached. A craniotomy was performed above the location of A1 as defined by autofluorescence imaging. The exposed brain was stabilized with a thin layer of 2% agarose (Sigma-Aldrich). After surgery, the anesthesia depth was controlled with MMF re-injections. During imaging experiments, the craniotomy was perfused with 37.5°C solution containing, in mM, 125 NaCl, 4.5 KCl, 1.25 NaH<sub>2</sub>PO<sub>4</sub>, 26 NaHCO<sub>3</sub>, 2 CaCl<sub>2</sub>, 1 MgCl<sub>2</sub>, 20 glucose at pH 7.4. Temperature and breathing rate of anesthetized mice were monitored continuously throughout the experiment.

### Autofluorescence imaging

A binocular microscope (MVX10, Olympus) equipped with a 0.63 x, 0.15 NA objective (MV PLAPO, Olympus), an Olympus U-M49002XL filter cube (excitation filter: 470/40 nm, dichroic mirror: 495 nm high pass, emission filter: 525/50 nm) and a CMOS camera (Zyla 4.2 Plus, Andor) was used to transcranially record flavoprotein fluorescence signals (Takahashi et al., 2006). The skull surface was covered with 0.9% NaCl solution to increase bone transparency and excited with a 470 nm LED (M470L2-C1, Thorlabs) using a light intensity of 4.2 mW below the objective. Images (128 × 128 pixels) were recorded at 10 Hz sampling rate with custom-written acquisition software (LabVIEW 2014, National Instruments).

### Two-photon imaging

We built a two-photon imaging setup specifically designed for auditory stimulation experiments and laser excitation wavelengths ranging up to 1200 nm. Acoustic noise from all measurement equipment was reduced with a custom-build sound-attenuation cage to below 20 dB in the relevant sound frequency range. The excitation sources were a pulsed fiber laser fixed at a wavelength of 1070 nm and a pulse width of 55 fs (Fidelity, Coherent) and a tunable pulsed infrared laser (InSight DeepSee, 80 MHz, Spectra-Physics or Coherent Discovery, Coherent) used for recordings with wavelengths ranging from 920-1200 nm and laser pulse widths below 120 fs. An electrically movable mirror (Thorlabs) was used to switch between both lasers. To reduce acoustic noise levels, the laser cooling unit of the tunable laser was moved to a separate room. Laser intensity was controlled with a laser modulator (Conoptics Model 302). Laser spot size was adjusted with a beam expander (BE02M-B; Thorlabs). A resonant scanning mirror with a resonance frequency of 12 kHz and a standard galvanometric mirror (Cambridge Technology) were used for scanning the fast and slow image axis, respectively. We also reduced the acoustic scanner noise to below 20 dB SPL using sound-dampening materials and additional casing for the scanner box. The scanning beam entered the chassis of the microscope (Olympus, BX51WI) through a scan-lens optimized for wavelengths up to 1050 nm (AC508150BML, Thorlabs). A dichroic mirror (F73-705, AHF Analysentechnik) separated excitation and emission by reflecting 710-1500 nm and transmitting 400-680 nm. The maximum laser power under the water-immersion objective (40 x, NA 0.8, Nikon Corporation) ranged from less than 20 mW in L2/3 to a maximum of 120 mW in L6 for depths around 800 μm below the cortical surface. A hybrid photo detector R7110U-40 (Hamamatsu) with a DHPCA-100 amplifier (FEMTO Messtechnik GmbH) was used to detect fluorescence signals. The microscope was controlled by custom-written software (LabVIEW 2014, National Instruments). Images were recorded at a frame rate of 40 and 80 Hz. The depth of each imaging region below the brain surface was verified with a z stack covering the depth from the respective region to the cortical surface. The depth of cortical layers was defined using published anatomical (Anderson et al., 2009) and functional data (Christianson et al., 2011). Key parameters of the two-photon imaging conditions used in this study (Birkner et al., 2017; Tischbirek et al., 2015) were chosen for long recording durations (> 90 minutes total illumination time) at the same cortical location in the absence of apparent heat-related damage in the upper cortical layers, which are most endangered by the laser illumination (see representative field-of-views in Figure 3A).

### Dye loading

A modified approach for multicell bolus loading (Stosiek et al., 2003) was used to label all cortical layers. 50 μg Cal-590 or Cal-520 AM (both AAT Bioquest) was dissolved in 4 μL DMSO + 20% pluronic-127. The dye was diluted with solution containing, in mM, 150 NaCl, 2.5 KCl, 10 HEPES at pH 7.4 to a final concentration of 500 μM. To facilitate loading, 25 μM Alexa680 (Sigma) was also included in the solution. 3-5 MΩ loading pipettes were made with a vertical puller (PC-10; Narishige Co., Ltd.) from borosilicate glass capillaries (Hilgenberg GmbH) and filled with 5-10 μl dye solution. The pipette angle was adjusted to be as steep as possible (34-37°) while still allowing two-photon imaging of the pipette tip. The pipette was inserted into the cortex with a micromanipulator (Luigs + Neumann) and guided to the required depth under two-photon guidance. Pressure (50-150 mbar, 1 min) was applied to the pipette to eject dye solution. The size of the labeled region was controlled by monitoring the Alexa680 fluorescence as a critical parameter for imaging quality (Birkner et al., 2017). After an incubation time of 1 hour, imaging experiments were performed. For additional labeled regions, the procedure was repeated with subsequent labeling sites either above or next to the original imaging location.

### Electroporation

Alexa680 or Alexa594 (Sigma) were dissolved to a 1 mM concentration in solution containing, in mM, 35 K-Gluconate, 4 KCl, 10 HEPES, 10 Na<sub>2</sub>Phosphocreatine, 4 Mg-ATP, 0.3 Na-GTP at pH 7.4. A 5–7-MΩ borosilicate glass pipette filled with dye was guided close to the desired layer 5 neuron. As electroporation was performed on neurons previously labeled with Cal-590 AM, target cells were readily identified under two-photon guidance. Two squared current pulses (270 nA, 30 ms) were applied to the pipette, using a custom-built amplifier in combination with a pulse stimulator (Isolated Pulse Stimulator Model 2100, A-M Systems). Z stack reconstructions were recorded 30 minutes after the electroporation.

### Auditory stimulation

Auditory stimulation was controlled using custom-written software (LabView). Acoustic stimuli were presented to the mouse through an electrostatic loudspeaker driver and loudspeaker (ED1, PA5, Tucker Davis Technologies) placed ~5 cm from the contralateral mouse ear. To localize A1, sequences of six pure tone bursts (100 ms duration with 10 ms on and off linear ramps, 200 ms inter-stimulus interval, 55 dB SPL) with 4 and 32 kHz were presented alternatively 20 times each, with an interval of 10 s between them. For two-photon imaging experiments, sequences of randomly ordered pure tones with 19 frequencies (2–45.3 kHz) at 5 attenuation levels (20–70 dB SPL) were used. Tones had a 100 ms duration (including 10 ms on and off linear ramps) and an inter-tone interval of 1500 ms. Each frequency-attenuation combination was presented 8–10 times. Background noise generated by the recording hardware, especially the resonance scanner of the two-photon microscope, was measured to be below < 20 dB SPL for the relevant frequency range.

### Electromyographic (EMG) recordings and analysis

EMG recordings were made with a pair of silver ball surface electrodes from the dorsal neck muscles. EMG signals were amplified with a gain of 100 using an AC amplifier (rpi Electronic), digitized at 12 kHz, and filtered by digital bandpass filter at 20 to 200 Hz. Periods of wakefulness were identified by high-amplitude, phasic EMG activity.

## QUANTIFICATION AND STATISTICAL ANALYSIS

Data analysis was performed using custom-written software in LabVIEW 2014 (National Instruments) and MATLAB version R2013a and R2014b (Mathworks).

### Autofluorescence imaging data analysis

The ΔF/F value of each pixel was calculated as the mean pixel fluorescence value for 10 frames (starting 5 frames after stimulation onset) divided by the mean of 10 frames before the stimulation. The resulting ΔF/F images were averaged for 20 trials per stimulation condition and filtered with a Gaussian filter (7 pixel diameter) to reduce spot noise. The brain surface tonotopy of A1 was estimated from autofluorescence imaging data by spatial linear interpolation of the 4 and 32 kHz-responsive regions. The line connecting the center points of the responsive regions was defined as the tonotopic axis.

### Two-photon imaging data processing

To extract Ca<sup>2+</sup> traces from raw recorded data, the average fluorescence value of manually selected regions of interest (ROIs) was used to calculate time series. For the correction of fluctuating background fluorescence levels, the out-of-focus neuropil signal was calculated as the average fluorescence value of an area surrounding each individual regions of interest, and subtracted from the time series after multiplication with a contamination ratio as described before (Hagihara et al., 2015; Kerlin et al., 2010). We calculated a contamination ratio independently for each imaging plane in each experiment. The variance of neuropil fluorescence in each imaging field of view was not statistically different between superficial (L2/3) and deep (L6) layers (two-sided t test, n = 7, p = 0.1998). For each ROI, the baseline fluorescence value F was calculated as the 10% median absolute deviation (MAD) of a 31 s time series. For each time point, a ΔF/F value was calculated. The resulting time course was low-pass filtered by a finite impulse response filter designed by the Parks-McClellan algorithm of the MATLAB function ‘firpmord’. The pass and stop frequencies of the filter were 22 and 12 Hz. The signal was subsequently bandstop-filtered (9.5 - 10.5 Hz). To preserve temporal features of the Ca<sup>2+</sup> signal, zero-phase filtering was used (MATLAB function ‘filtfilt’).

### Active ROIs

To detect “active” neuronal ROIs, the filtered ΔF/F time course was further high-pass filtered (0.4 Hz) to remove slow trends and normalized using the median and MAD of the ΔF/F distribution. In the normalized series, local peaks were detected with the MATLAB function ‘findpeaks’. The corresponding transients were kept for further processing if the peak normalized scores were > 3.45 (corresponding to a z score of 2.33) and if the normalized difference between onset time and peak time was greater than 2. The onset of a Ca<sup>2+</sup> transient was considered to be the time interval between the time of the last trough preceding the peak and the time of the peak. Next, to detect “active” ROIs, peak and decay integral ΔF/F values were determined (Rothschild et al., 2010). Peak ΔF/F was calculated as the difference of ΔF/F between Ca<sup>2+</sup> transient onset and the peak value. Decay integral ΔF/F was defined as the time integral of ΔF/F values from the Ca<sup>2+</sup> transient peak time point to 300 ms thereafter. Peak and decay integral ΔF/F distributions of each ROI were converted into normal distributions by a Box-Cox transformation (exponents λ = 0.75 ± 0.40 and λ = 0.27 ± 0.75 for peak and

decay integrals). A neuronal ROI was considered as active (within recording durations of at least 900 s) when at least one event in the transformed  $\Delta F/F$  distribution of  $\text{Ca}^{2+}$  transients was  $\geq 25$  Mahalanobis distances from the  $\Delta F/F$  values in a selected “inactive” neuropil/blood vessel ROI.

#### Responsiveness to pure tones

To calculate the amplitude of tone-evoked  $\text{Ca}^{2+}$  transients, the average prestimulus baseline  $\Delta F/F$  value ( $-300\text{-}0$  ms) was subtracted from the average poststimulus peak  $\Delta F/F$  value ( $20\text{-}320$  ms) of all trials. ROIs were defined as “responsive” if a tone-evoked  $\text{Ca}^{2+}$  transient showed a statistically significant effect of stimulus ( $p < 0.05$ ) as determined by a one-way ANOVA of all 95 frequency-intensity conditions. ROIs were defined as silent when they showed no clear  $\text{Ca}^{2+}$  transient during the entire recording duration. ‘Irregular’ ROIs are both non-responsive neurons, which showed spontaneous  $\text{Ca}^{2+}$  transients, and responsive neurons with significant response to sounds, which showed no clear but diffuse FRA with multiple weak responses distributed over a large number of tone frequency and intensity combinations (Guo et al., 2012; Moshitch et al., 2006).

#### Frequency response area analysis

The frequency response area (FRA) of each ROI was defined by grouping responsive frequency-intensity conditions. To determine if a frequency-intensity condition was responsive, two criteria were combined: the response had to show a significant change of the poststimulus signals from prestimulus signals (Wilcoxon’s signed rank test,  $p < 0.05$ ), and the response had to occur in at least 30% of the trials. A response was considered to occur in a single trial when the poststimulus time-averaged signal was at least 3 standard deviations higher than the pre-stimulus baseline.

Tuning curves (boundaries of FRAs) were constructed from edges of the responsive frequency-intensity conditions, that is, adjacent responsive and non-responsive frequency-intensity combinations. In order to verify the plausibility of the obtained tuning curves, all FRAs were inspected visually and about 85% of the cases achieved clear FRA boundaries. The best frequency (BF) of a FRA was determined by averaging responses at each frequency over all sound levels and selecting the frequency where the average response was maximal. We computed the response quality  $d'$  (Guo et al., 2012) for a comparison of response-to-background levels across layers. The response level was defined as the trial-by-trial response magnitude across frequency-intensity combinations within the FRA, and the background level as trial-by-trial response magnitude outside the FRA, respectively (Noda and Takahashi, 2015). We randomly chose fixed number of conditions (e.g., 50) and calculated the average z-scores over the conditions, separately for each response/background level. This procedure was repeated 500 times to correct for statistical bias, and two sets of bootstrap data with 500 samples in both levels were made. The statistical distance of distributions between the responsive level and background level was quantified based on the equation used by Guo et al. (2012).

Bandwidth<sub>20</sub> is defined as a distance in octave at 20 dB above minimum threshold of the FRA, between the highest frequency and the lowest frequency of the FRA boundary where the neuron had significant responses, following a standard way in the field (Moshitch et al., 2006; Schreiner and Sutter, 1992). Best-level bandwidth is the bandwidth at the best intensity level, which elicits the strongest response among all intensity levels at the best frequency.

The minimum intensity threshold was the highest attenuation where a significant tone response occurred. To calculate the sharpness of frequency tuning, the bandwidths at different attenuation levels above the minimum threshold were determined from the tuning curve.

#### Analysis of BF distribution

To compare the BF heterogeneity between layers, we analyzed the BF distribution in fixed-size analysis windows ( $200 \mu\text{m} \times 130 \mu\text{m}$ ) in all layers. The BF heterogeneity was quantified by the 90% trimmed range ( $R_{90}$ ) and inter-quartile range of the distribution (Winkowski and Kanold, 2013).

#### Micro-tonotopy

To evaluate the tonotopy in local regions, a BF gradient vector (Guo et al., 2012) was calculated for each pair of frequency-tuned neurons. The BF gradient vector was defined as the BF difference of between neuron  $i$  and neuron  $j$  in octaves, normalized by the Euclidean distance between the location of neuron  $i$  and that of  $j$ , multiplied by a unit vector directed from the location of neuron  $i$  to neuron  $j$ . The “micro-tonotopic gradient” was defined as the vector average of all BF gradient vectors in the fixed-size imaging field of view with at least 7 neurons. The “micro-tonotopic axis” was defined as the axis along the average vector.

#### Alignment of layers

Imaging regions in separate layers were aligned to each other according to a vector defined by the dendritic trunk axis of electroporated layer 5 neurons. The coordinates to calculate the vector were extracted from two-photon z stacks recordings as the average of at least 3 different dendrites using the ImageJ Plugin Simple Neurite Tracer (Longair et al., 2011). For the comparison of tone-response properties across different layers, only aligned regions of overlying layers were included in the data analysis. Layer 6 was aligned by extrapolating the dendritic trunk vector of the overlying layers to the layer 6 imaging depth.

#### Significant BF change

To quantify the BF consistency within a region size of a few hundred  $\mu\text{m}$ , we calculated the distance at which a significant change of the BF distribution occurred. We tested the distance along the micro-tonotopic and isofrequency axes in the same region, respectively. First, the BF distribution was determined for two separate analysis windows, which had a variable length (30–90  $\mu\text{m}$ ) parallel to the tested axis and a fixed length (130  $\mu\text{m}$ ) vertical to the tested axis. Second, the difference between the means of the distributions of BFs in the two analysis windows was tested with a two-sample t test. The distance between the centers of the two windows increased in 10  $\mu\text{m}$  steps. To reduce the effect of a specific sample size in each window, the test was repeated with window sizes

ranging from 30 to 90  $\mu\text{m}$ , and the median of the distance with the first significant BF difference for the different window sizes was calculated.

#### ***Image processing***

Solely for illustrative purposes, ImageJ was used for contrast adjustments of raw two-photon average images. Adobe Photoshop CS5 was used to adjust the brightness and contrast of the skull surface image ([Figure 1B](#)), and to create overlay images of autofluorescence data. Aligned imaging data ([Figure 4A](#)) was visualized with Amira 6.0 (FEI, Thermo Fisher Scientific).